RAI Volume 3, Chapter 2.2.1.3.1, Second Set, Number 3, Supplemental:

Explain whether or not the test conditions and unexpected results described in CRs 12799 and 12868 affected the samples and data used to derive corrosion rates discussed in SAR Section 2.3.6.3 and the recleaned specimens test data discussed in DOE's responses to RAIs 3.2.2.1.3.1-2-003 and 3.2.2.1.3.1-2-004. If the SAR and recleaned specimen data were affected by the test conditions described in the CRs, discuss the impact on the Performance Assessment.

Additional questions:

1. Clarify the number of 5-year test specimens affected by the unexpected conditions described in CR 12799 and CR 12868.

2. Clarify if the assessment will include details for the 5-year corrosion rate data.

3. Clarify if there is any overlap between the oxide deposits identified in CR 12799 and carbon deposits in CR 12868.

4. Clarify if the cleaning procedures used in both CRs are consistent with cleaning procedures in DOE's response to Set 2, RAI #3.2.2.1.3.1-2-003.

1. SUPPLEMENTAL RESPONSE

Condition report (CR) 12799, "Unexpected Test Results - Heterogeneous Alloy 22 Oxide Thickness," addresses a locally thicker oxide coating observed on weight loss coupons in regions which were covered by an inert washer while exposed within the Long Term Corrosion Test Facility (LTCTF). CR 12868, "Unexpected Test Results - Residue on Subset of Alloy 22 Coupons," focuses on the nature of an organic layer which was initially observed on un-cleaned Alloy 22 coupons from the 9.5-year test interval in the LTCTF. Although the test conditions and results of these two CRs affect the samples and data used to derive corrosion rates discussed in the SAR (Section 2.3.6.3 and the re-cleaned specimen test data discussed in DOE's response to RAI 3.2.2.1.3.1-2-003), the magnitude of the effect is insignificant in terms of the general corrosion rates determined from the coupons. Furthermore, the issues identified in both CRs are believed to have a negligible impact on both performance assessment and criticality analyses, and will be subject to further confirmation as discussed herein.

1.1 REVIEW OF DATASET DISCUSSED IN THE RESPONSES TO RAI 3.2.2.1.3.1-2-003 AND RAI 3.2.2.1.3.1-2-004

1.1.1 RAI 3.2.2.1.3.1-2-003

The Alloy 22 general corrosion rate data presented in *General and Localized Corrosion of the Waste Package Outer Barrier* (SNL 2007) as well as SAR Section 2.3.6.3 are based upon crevice coupons exposed for five years in the LTCTF. In addressing CR 11851, "Unexpected Cleaning Weight Loss of Alloy 22 Control Samples," it was established that due to variations in the surface finish of the crevice coupons, they are inappropriate to use as a representation of the

Alloy 22 general corrosion rate, as their corrosion rate (determined via weight loss) is dominated by experimental artifacts and therefore does not accurately represent the Alloy 22 general corrosion rate. As a result, the weight loss coupons (which do not have this surface finish artifact) were re-cleaned, and present a more accurate representation of the Alloy 22 general corrosion rate.

The distribution of corrosion rates from the five-year re-cleaned weight loss coupons has a lower median value and narrower spread relative to the Alloy 22 general corrosion model (a Weibull distribution based on the (not re-cleaned) crevice coupon data) presented in the SAR (see the response to RAI 3.2.2.1.3.1-2-003). Analyses continue for the update to *General and Localized Corrosion of the Waste Package Outer Barrier* (SNL 2007), and will include fitting the distribution of re-cleaned weight loss coupon general corrosion rates and confirm the current assessment of its impact on performance assessment results.

1.1.2 RAI 3.2.2.1.3.1-2-004

The response to RAI 3.2.2.1.3.1-2-004 presents a summary of the results from a series of new and previously available studies and analyses used to determine the uncertainties associated with the long-term persistence of the passive film on Alloy 22 with regard to the structure, composition, and thickness of the passive film. These studies conclusively demonstrated the long-term stability of the passive oxide film on Alloy 22 under a wide range of repository-relevant conditions. The studies above included experimentation performed to improve the understanding of the impact that silica scale, or other foreign matter, might have on the oxide stability, and therefore the general corrosion rate, of Alloy 22. The data indicates that silica deposited on the surface of the Alloy 22 coupons during exposure to silicate-bearing solutions does not have a discernable impact on the stability of the passive oxide, and hence the general corrosion rate, of Alloy 22.

1.2 COUPONS DIRECTLY IMPACTED BY THE PHENOMENA DESCRIBED IN CR 12799 AND CR 12868

The two CRs in question apply to *all* of the coupons that were exposed within the LTCTF (i.e., both the crevice coupons presented in the SAR and the re-cleaned weight loss coupons discussed in the response to RAI 3.2.2.1.3.1-2-003); however, the magnitude of the two CRs' impact is insignificant in terms of the general corrosion rates determined from the aforementioned coupons.

The experiments which form the basis of the response to RAI 3.2.2.1.3.1-2-004 are a series of independent electrochemical experiments that were not performed in the LTCTF tanks. As such, neither CR 12799 nor CR 12868 is applicable to the discussion presented in that response.

1.3 IMPACT OF CR 12799 (HETEROGENEOUS ALLOY 22 OXIDE THICKNESS) ON PERFORMANCE ASSESSMENT

A conservative estimate of the impact which the heterogeneous oxide layer thickness reported in CR 12799 will have on the Alloy 22 corrosion rates used in the performance assessment indicates that the effective change in corrosion rate is less than the uncertainties applied. The following discusses the basis for that conclusion.

While analyzing the surface of corrosion test coupons taken from the LTCTF after they had been cleaned, it was noted that the surface oxide appeared optically irregular, with both light and dark regions visible. These regions corresponded predominantly to the location where the polytetrafluoroethylene (PTFE) spacer used between coupons made contact with the coupon surface, and consisted of approximately 3% of the total surface area of each coupon (see Figure 1). The cleaning process utilized to prepare these coupons is described in the response to RAI 3.2.2.1.3.1-2-003, Section 1.2 (Specimen Re-Cleaning).

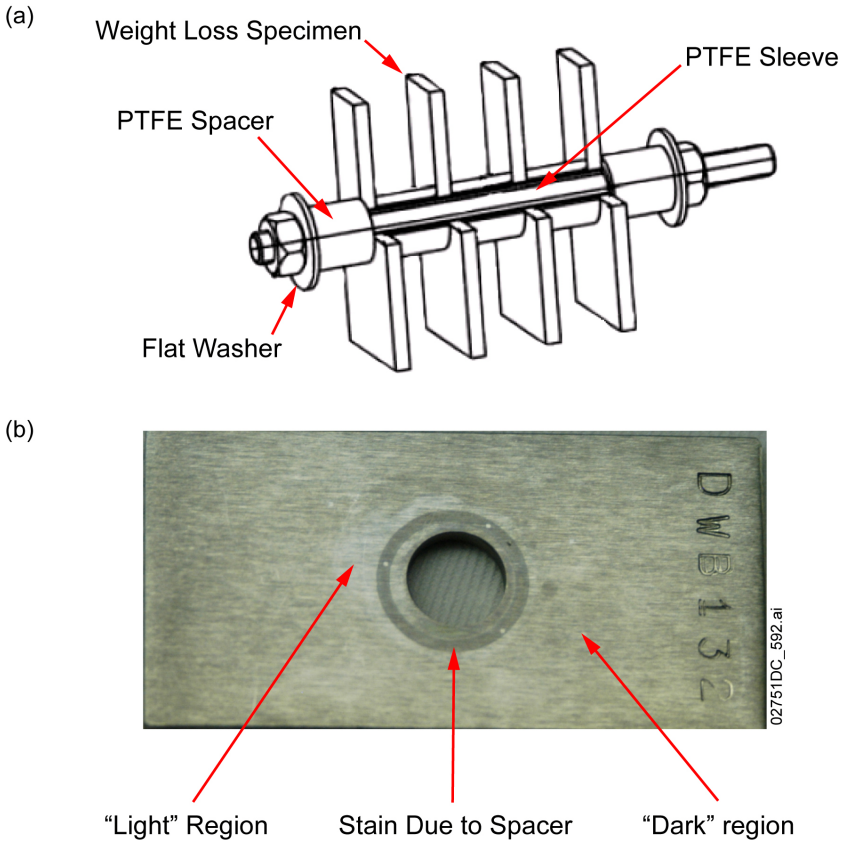

NOTE: The light "spots" in the stain due to the spacer are regions where the oxide was sputter depth profiled for the evaluation of CR 12799.

Figure 1. (a) Weight Loss Coupon Assembly from the LTCTF Illustrating Where the Spacers Were Located; (b) Optical Image of a Re-Cleaned Weight Loss Specimen Illustrating the Locally Dark Regions on the Specimen Surface

Corroborative, non-Q, secondary ion mass spectrometry (SIMS) analysis revealed a locally thicker oxide in the dark region corresponding to where the spacer had contacted the coupon (see Figure 1B). The oxide thickness in the regions below the PTFE spacer was evaluated on both 5- and 9.5-year specimens taken from the LTCTF, the results of which are summarized in Table 1.

Table 1. Comparison of Average Oxide Thickness for Various Sites on Alloy 22 Coupons as a Function of Immersion Time in 90°C SCW

Time (yr)	Location	Oxide Thickness (nm)
5	Light	7
	Dark	14
	Washer	159
9.5	Light	17
	Dark	204
	Washer	409

An evaluation of the structure of the regions where the locally thicker oxide was present revealed no signs of enhanced general corrosion or localized corrosion. Compositionally, however, the oxide layer in the thick regions below the contact area between the PTFE spacer and the metal surface differed from the oxide layer present on other portions of the surface. The thickened oxide contained elevated concentrations of chloride, magnesium, silicon (as a silicate), and carbonaceous species. The chemical composition of these deposits strongly suggests that they are the result of deposition from solution (i.e., deposit of solution components or corrosion product from other less corrosion resistant materials that were present in the same exposure vessel, such as Incoloy 825, which did exhibit significant corrosion), as many of the species present in the thick oxide layer are not present in the parent metal, and no signs of enhanced dissolution were observed. This conclusion is also supported by the greater thicknesses observed for the darker regions on the 9.5-year coupons.

While the likely cause of the increased oxide layer thicknesses is the formation of a deposit from the exposure solution, and no signs of enhanced corrosion were observed, the presence of the thicker oxide deposit can have an impact on the weight-loss measurements. The mass of the thicker oxide layer can reduce the measured weight loss (i.e., it represents material which should have been removed) relative to what the measured weight loss would be if the thicker oxide layer were completely removed. To estimate the impact this deposit would have on the measured weight loss, and hence the calculated corrosion rate, the mass of the deposit can be estimated, and then converted into an equivalent change (increase) in corrosion rate. Utilizing a deposit thickness of 200 nm (slightly larger than the average deposit thickness of 159 nm (see Table 1)), and assuming that 5% of the surface area of each coupon is impacted (rather than the ~3% observed), the weight increase due to the presence of the thick oxide layer, ΔW, can be calculated as:

$$\Delta W = \left(SA_{coupon}\right) \times \left(Coverage\right) \times \left(t_{oxide}\right) \times \left(\rho_{oxide}\right)$$

where the total surface area of a weight-loss coupon, SA_{Coupon}, is 30 cm^2, *Coverage* is the portion of the surface area coated with the thicker oxide layer (5%), the thickness of the deposit, t_{oxide}, is 200 nm, and the density of the oxide layer, ρ_{oxide}, is 5.21 g/cm^3 (assume the oxide is entirely Cr_2O_3), yielding a weight change of 156 µg. This weight change can then be converted to an equivalent increase in corrosion rate, ΔCR (in nm/yr), of:

$$\Delta CR = \left(\frac{\Delta W}{\rho_{Alloy\ 22}}\right) \times \left(\frac{1}{SA_{Coupon}}\right) \times \left(10^7\ \frac{nm}{cm}\right) \times \left(\frac{1}{Exposure\,time}\right)$$

where the density of Alloy 22, $\rho_{Alloy\ 22}$, is 8.69 g/cm^3 and the exposure time is 5 years. The "worst case" change calculated via this expression is approximately 1.2 nm/yr. This potential change in corrosion rate is less than half of the combined standard uncertainty of 2.49 nm/yr associated with the re-cleaned weight loss coupons, as presented in the response to RAI 3.2.2.1.3.1-2-003. Therefore, while the locally thick oxide regions will have an impact on the observed weight loss for each coupon, the magnitude of that change is less than the combined standard uncertainty for the measurement. As such, the impact of the issues identified in CR 12799 on performance assessment is negligible based upon the discussion above and the expected results of planned confirmatory work.

1.4 IMPACT OF CR 12868 (ORGANIC RESIDUE ON COUPONS TAKEN FROM LTCTF) ON PERFORMANCE ASSESSMENT

Inspection of uncleaned Alloy 22 coupons exposed for 9.5 years in the LTCTF revealed that a subset of the coupons has a visually observable organic residue on the sample surfaces and adhered to the inside of the plastic bags used for sample storage. Although the thickness of the organic layer varied on a given coupon surface, the organic layer was reasonably continuous (i.e., the deposit was not patchy in nature). This morphology is significantly different than the nonuniform/discontinuous heterogeneous oxide layer discussed in CR 12799, and as such it is unlikely that the phenomena reported in CR 12799 is related to the organic deposit discussed in CR 12868. Evaluation of the organic layer via a series of analytical techniques revealed that it was not the result of either tank wall degradation or biological activity, but rather was a long-chain hydrocarbon molecule consistent with a lubricant. The source of the contamination was identified as Mobilith SHC007, a high-temperature grease used in the gear box for each of the Baldor stirrer motors used to agitate the solution within each of the LTCTF tanks. A series of uncleaned coupons extracted at times prior to the 5-year sample period was evaluated via a Fourier transform infrared (FTIR) analysis, revealing that the organic layer was present as early as the 1-year mark (earliest sample time from which uncleaned coupons were available), gradually increasing in thickness over time, consistent with the probable source. It should be noted that the samples were stored for approximately three years in bags before this analysis was performed. As such, the organic layer may have redistributed across the surface of each coupon and a portion of the deposit on each sample surface may have been transferred to the inside surface of the bag in which it was stored, reducing the quantity on the surface at the time of the FTIR analysis.

A series of 9.5-year samples with varying organic layer thickness (based upon an initial visual evaluation) was further evaluated to determine a semi-quantitative measure of the quantity of organic residue on the surface, followed by using the current project procedures (the refined procedures used to re-clean the 5-year coupons described in the response to RAI 3.2.2.1.3.1-2-003, Section 1.2 (Specimen Re-Cleaning)) to establish the corrosion rate for each weight loss coupon. The results of the aforementioned process are presented in Figure 2. In addition, the average corrosion rate from the 5-year re-cleaned weight loss samples is plotted for comparison. As illustrated in the figure, no correlation was observed between the apparent quantity of organic residue present on the surface of a coupon and its corrosion rate. Based upon this observation, CR 12868 was closed, as there was no discernable impact of the organic layer on the corrosion rate.

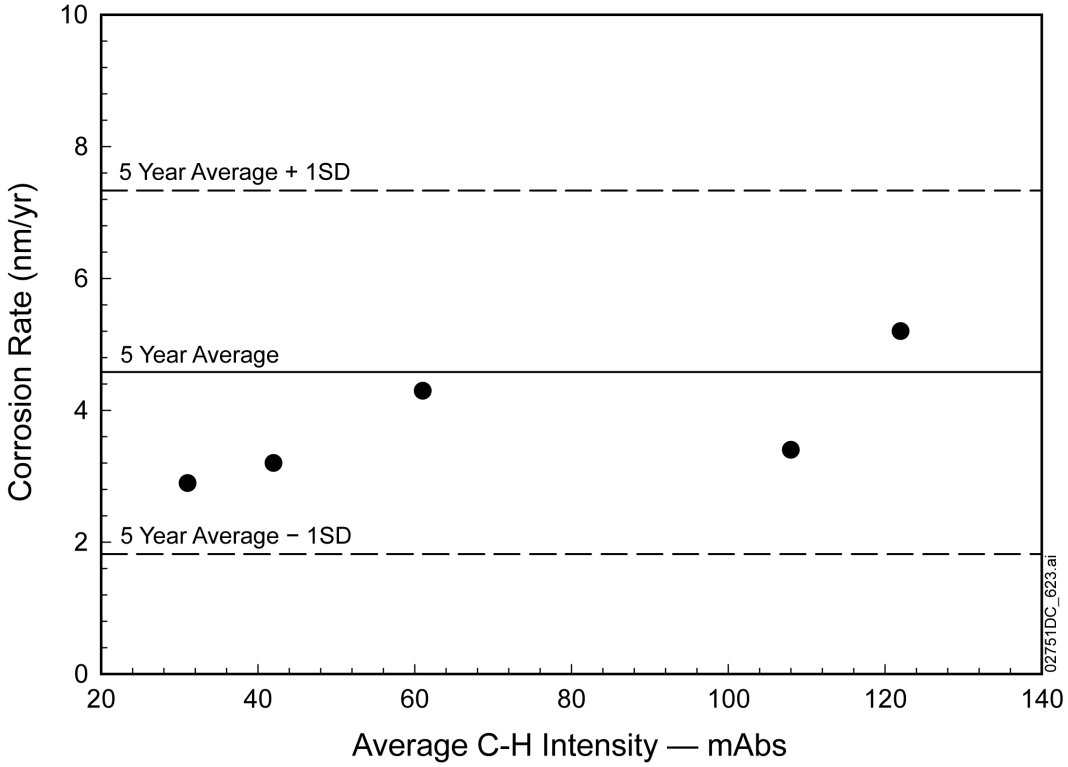

NOTE: For comparison, the average corrosion rate from the 5-year weight loss coupons is also plotted.

Figure 2. Corrosion Rate as a Function of Average C-H Intensity (approximately proportional to the quantity on the metal surface) from FTIR

In order for the organic layer to have an impact on the general corrosion process, it must hinder either the anodic reaction (i.e., metal oxidation), the cathodic reaction (i.e., oxygen reduction), or both. As Alloy 22 is a passive metal, and thus the dissolution rate is very small, it is unlikely that the anodic reaction rate is hindered by reduced mass transport due to the presence of the lubricant layer. Similarly, as the lubricant is a nonreactive compound (i.e., no surface active sites), it is unlikely that it is binding to, or reacting on, the metal surface, obscuring (and hence protecting) active sites and thereby reducing the anodic reaction rate. The most likely impact which the organic layer would have on the corrosion process would be the reduction of the

cathodic reaction rate by hindering the mass transport of oxygen from the aerated bulk solution to cathodic sites at the metal/solution interface.

If a bounding general corrosion rate of 25 nm/yr is assumed, the equivalent anodic reaction rate can be calculated. Using the expressions presented in ASTM G102, the corrosion rate in nm/yr can be converted to a current in A/cm^2 via manipulation of Equation 5 from ASTM G102:

$$CR = K_1 \frac{i_{corr}}{\rho} EW \quad \Rightarrow \quad i_{corr} = \frac{\rho \times CR}{EW \times K_1}$$

Using a corrosion rate, CR, of 25 nm/yr, a conversion factor K_1 of 3.27×10^{-3} mm*g/(µA*cm*yr), the density of Alloy 22, ρ, of 8.69 g/cm^3, and an equivalent weight, EW, for Alloy 22 of 23.28 (ASTM G102, Table 1), the corrosion current density would be 2.85 nA/cm^2. The total cathodic current is, by definition, equal to the total anodic current, so assuming the anodic and cathodic areas are equivalent, the cathodic current density is 2.85 nA/cm^2. Assuming that the cathodic reaction is oxygen reduction, the cathodic reaction will be hindered to the point it impacts the anodic reaction rate when the diffusion of dissolved oxygen to the metal surface is reduced to the point that the limiting current density of the oxygen reduction reaction becomes less than the cathodic reaction rate required to support the anodic reaction rate. The limiting current density for oxygen reduction can be calculated as:

$$i_L = \frac{nFDC^o}{\delta}$$

where i_L is the limiting current density, n is the number of electrons consumed by the reaction (2 for the reduction of each oxygen atom), F is Faraday's constant (96484.6 C/equivalent), D is the diffusivity of oxygen (10^{-5} cm^2/s), C^o is the bulk dissolved oxygen concentration (4 to 10 ppm), and δ is the thickness of the boundary layer, assumed to be 50 µm for this calculation. Given that the solubility of oxygen is higher in oil than in water (Tian and Cheng 2008), C^o may conservatively be set equal to the concentration in the water phase, which was measured as being between 4 and 10 ppm (see Farmer *et al.* 2000, p. 6) – using a concentration of 4 ppm, the limiting current density for oxygen reduction will be approximately 96 µA/cm^2. As the calculated limiting current density is approximately four orders of magnitude larger than what is required to support the passive dissolution of Alloy 22, it is clear that the organic layer will not impact the cathodic reaction rate such that the anodic reaction rate is reduced. Thus, it is unlikely that the presence of the organic layer on the Alloy 22 surface adversely impacted the cathodic reaction rate.

To summarize, it is anticipated that neither the anodic nor the cathodic reaction rate for Alloy 22 in the solutions utilized within the LTCTF were altered in a meaningful way by the organic layer present on the coupon surfaces. Therefore, the impact of the issues identified in CR 12868 on performance assessment is expected to be negligible. As such, the impact of the issues identified in CR 12868 on performance assessment is negligible based upon the discussion above and the expected results of planned confirmatory work.

1.5 SUMMARY

As discussed above, the issues identified in CRs 12799 and 12868 will have a minimal impact on the data used to derive the corrosion rates used in the SAR, and as such, the impact of both CRs on performance assessment is negligible. Furthermore, as there is minimal impact on the Alloy 22 general corrosion rate, there will be no impact to existing criticality analyses.

1.5.1 Clarify the Number of 5-Year Test Specimens Affected by the Unexpected Conditions Described in CR 12799 and CR 12868

All of the Alloy 22 coupons exposed in the LTCTF were impacted by both CRs.

1.5.2 Clarify If the Assessment Will Include Details for the 5-Year Corrosion Rate Data

The discussion in the initial RAI as well as the supplemental response presented here focus almost exclusively on the 5-year corrosion rate data.

1.5.3 Clarify If There Is Any Overlap between the Oxide Deposits Identified in CR 12799 and Carbon Deposits in CR 12868

The organic layer described in CR 12868 covered the entire surface area of the impacted test coupons – as such, the locally thicker oxide regions observed in CR 12799 were coated with the organic layer discussed in CR 12868.

1.5.4 Clarify If the Cleaning Procedures Used in Both CRs Are Consistent with Cleaning Procedures in DOE's Response to Set 2, RAI #3.2.2.1.3.1-2-003

Identical cleaning procedures were used for the datasets presented in the original and supplemental responses to RAI 3.2.2.1.3.1-2-003.

2. COMMITMENTS TO NRC

The impact of CR 12799 and CR 12868 on the updated general corrosion rate data described in response to RAI 3.2.2.1.3.1-2-003 will be documented in the revision of SAR Section 2.3.6 promised in the aforementioned RAI. The change to the SAR will be included in a future license application update.

3. DESCRIPTION OF PROPOSED LA CHANGE

SAR Section 2.3.6.3 text will be revised to include a discussion of the heterogeneous oxide layer discussed in CR 12799 and the organic deposits discussed in CR 12868. The change will be included in a future license application update.

4. REFERENCES

Farmer, J.; McCright, D.; Gdowski, G.; Wang, F.; Summers, T.; Bedrossian, P.; Horn, J.; Lian, T.; Estill, J.; Lingenfelter, A.; and Halsey, W. 2000. "General and Localized Corrosion of Outer Barrier of High-Level Waste Container in Yucca Mountain." UCRL-JC-138890. Livermore, California: Lawrence Livermore National Laboratory.[a]

SNL (Sandia National Laboratories) 2007. *General Corrosion and Localized Corrosion of Waste Package Outer Barrier*. ANL-EBS-MD-000003 REV 03. Las Vegas, Nevada: Sandia National Laboratories. ACC: DOC.20070730.0003.

Tian, B.R. and Cheng, Y.F. 2008. "Electrochemical Corrosion Behavior of X-65 Steel in the Simulated Oil Sand Slurry. I: Effects of Hydrodynamic Condition." *Corrosion Science*, *50*, 773-779. New York, New York: Elsevier.

NOTE: [a]Provided as an enclosure to letter from Williams to Cuadrado, dtd 9/10/2009, Yucca Mountain - Request for Additional Information - Safety Evaluation Report, Volume 3 - Postclosure Chapter 2.2.1.3.1 - Degradation of Engineered Barriers 4th Set - (Department of Energy's Safety Analysis Report Section 2.3.6.8)

RAI: Volume 3, Chapter 2.2.1.3.3, First Set, Number 7, Supplemental:

Transport in the NFC model is calculated using a plug flow approximation. Provide technical bases that demonstrate using average hydraulic properties in the NFC model appropriately captures the variability and uncertainty in seepage water compositions expected in the repository environment. Consider the impact of variable flow rates on potentially aggressive seepage water chemistry as influenced by water residence times and feldspar dissolution rates.

Basis: Transport through the NFC model domain is modeled using a plug flow approximation. This approach treats the TSw as a homogeneous 200-m thick column with properties averaged from the four TSw repository host units (weighted average based on thickness). This approach includes combining and averaging matrix and fracture hydrologic properties and ignores the possibility of fast flow, via fractures, through the model domain. As a result, the range of residence times predicted by the model may not appropriately capture the potential range in water residence times in the repository environment. The residence time directly affects the amount of feldspar that dissolves in seepage water, which in turn affects the compositional range and corrosivity of seepage water.

1. RESPONSE

The effective residence time approximation in the near-field chemistry (NFC) model is used with average hydraulic properties and variable flow rates, and implemented with a plug-flow calculation, to appropriately represent the variability and uncertainty in seepage water composition. The response emphasizes the role of the active fracture model (AFM) to represent fast pathways in simulations that support the NFC model, and presents corrected simulations that demonstrate the extent of fracture-matrix interaction in the host rock. Numerical simulations of tracer transport using the AFM, over a range of percolation flux, are used to calibrate the effective transport velocity (implemented in a plug-flow calculation) that controls the extent of water-rock interaction in the NFC model.

The original simulations using the FEHM code are compared to corrected simulations developed using T2R3D V. 1.4 (used with TOUGH2 V. 1.6), a process-level simulator that was also used to support the unsaturated zone (UZ) transport model for the performance assessment (SAR Section 2.3.8.4.2). These results show that the plug-flow feature of the NFC model, when calibrated to numerical results that include rapid breakthrough behavior at higher percolation flux values, is a reasonable approximation for the effective residence time or transport velocity of solute in waters percolating through the host rock. Using the breakthrough curves based on the T2R3D representation of flow, the potential range in water residence times and the associated range in composition of seepage water are represented.

Other sources of variability and uncertainty in the NFC model are also propagated in the total system performance assessment for the license application (TSPA-LA) through use of ranges for host-rock thermal conductivity, feldspar dissolution rate, and thermal history associated with

location in the repository. These features of the model are discussed in more detail in the response to RAI 3.2.2.1.3.3-002.

1.1 REPRESENTATION OF FAST PATHWAYS

The unsaturated zone flow model is described in SAR Section 2.3.2, particularly flow through the TSw unit (SAR Section 2.3.2.2.1.3), fracture-matrix interaction (SAR Section 2.3.2.2.2.1), effects from major faults (SAR Section 2.3.2.2.2.2), and isotopic evidence (SAR Section 2.3.2.3.4.3). The section on flow focusing (SAR Section 2.3.2.2.2.3) observes that while focusing of fracture flow occurs throughout the host rock and is not limited to major faults, the distribution of focused flow paths in the unfaulted regions is relatively uniform. This is based on measurements of average liquid saturation and *in situ* water potential, which exhibit limited variability throughout the host rock. Thus, it is appropriate to represent the unsaturated zone as a layered, porous (dual-permeability) medium with uniform properties within rock units.

The existence of preferential fracture flow pathways throughout the host rock is represented in the UZ flow model using a dual-permeability (DKM) approach, with preferential flow through a subset of the total fracture population represented by the AFM. The DKM approach allows disequilibrium of water potential in fractures relative to the nearby rock matrix. The AFM represents gravity-dominated, nonequilibrium, preferential liquid water flow in fractures, similar to fingering in unsaturated porous media. These focusing effects are represented in the simulations used in calibrating the NFC model effective residence times, which is important because the effects realistically increase the velocity of fracture flow and decrease the interfacial area for fracture-matrix interaction.

1.2 AFM SIMULATIONS FOR THE NFC MODEL

Numerical simulations of tracer transport in the fractured host rock were used for calibrating the effective residence time approximation implemented in the NFC model. This approximation represents residence time of the solute in potential seepage water, rather than the water itself. Plug-flow is an aggregation of fast and slow pathways that implies physical and chemical equilibrium between the pathways. However, for the NFC model, “plug-flow” is implemented by choosing a percolation flux that produces the effective residence time calculated from numerical transport simulations. The residence time for solvent water in the fractures is less than the effective residence time for solute, and the residence time for solvent water in the rock matrix is greater than the effective residence time for solute.

If inflowing fracture water at the top of the column were assigned the same composition as water in the matrix, then no compositional changes would occur in the column, and no breakthrough would be observed at the bottom. The breakthrough time thus expresses the average latency that occurs for any difference in composition of the inflowing water. The latency is caused by direct migration of solute into and out of the rock matrix, and is represented by the residence time, which approximates the time spent in the rock matrix. It also represents the water–rock interaction time available for solutes that originate in the matrix and diffuse into the fractures.

In a slowly varying system that has achieved a dynamic steady state, the fracture and matrix water compositions are locally constant (but may vary with depth). Considering a small control volume containing matrix and fractures, the local production of solutes such as Na^+ and K^+ in the matrix is transported by diffusion to the fractures. Conversely, if a different solute such as Ca^{2+} is provided by fracture flow from above, the net solute influx to the fracture volume, i.e., influx minus outflux, is transported by diffusion to the matrix. The residence time for the control volume then corresponds to the average duration of transport from matrix and fractures (or vice versa) at the local, steady rate of production (or rate of net influx). The residence time for the column is obtained by integrating along the flow path. This situation is analogous to the effective residence time as represented in the NFC model, assuming the local compositions of fracture and matrix waters to be in quasi-steady state (but not necessarily in chemical equilibrium). The local rate of solute production in the matrix (or net solute influx in fractures) varies slowly with the local temperature, and with percolation flux.

The transport simulations described in SAR Section 2.3.5.3 were performed using FEHM V. 2.24 in a manner similar to one-dimensional validation cases used in support of the abstraction of unsaturated zone transport for the TSPA-LA (SAR 2.3.8.5; SNL 2008, Figures 7-2 to 7-7). Description of the original FEHM simulations used to develop the NFC model is provided in SAR Sections 2.3.5.3.2 and 2.3.5.3.3, as well as the model report (SNL 2007a, Sections 6.3.2.3 and 6.3.2.4.4). This response presents simulations using the T2R3D code, that correct recently discovered errors with specification of fracture spacing, aperture, and permeability in the implementation of the AFM in the original FEHM runs. In Section 1.3 the impact on the predicted composition of fracture waters is evaluated by implementing the breakthrough curves based on the T2R3D representation of flow and transport. This results in changes to the concentrations of major cations by a few parts per million. These changes are only observed at higher values of percolation flux. An important difference between the FEHM and T2R3D codes in this application is that T2R3D incorporates the AFM in both flow and transport using full numerical implementation of the differential equations for flow and transport, whereas FEHM generates non-AFM flow fields and then implements AFM in transport using particle tracking.

For reference in this response, the key transport and hydrologic parameters of these simulations are shown in Tables 1 and 2. Calculation of the effective residence time, or “plug-flow transport time,” and the associated velocity is described in SAR Section 2.3.5.3.3.2.7. The simulations presented and compared in this response are summarized in Table 3. The T2R3D simulations used the same transport and hydrologic properties, implementing the AFM in flow calculations as well as transport, and resulting in breakthrough curves which are plotted in Figure 1 and summarized in Table 4.

Table 1. Transport Parameters for FEHM and T2R3D Simulations used with the NFC Model

Hydrologic Unit	Unit Bottom Elevation (m)	Unit Top Elevation (m)	Unit Thickness (m)	Fracture Half-Spacing (m)	Active Fracture γ (Notes 1, 2)
tsw31	1,279.7	1,294.1	14.4	0.46	0.4
tsw32	1,249.3	1,279.7	30.4	0.89	0.4
tsw33	1,169.2	1,249.3	80.1	1.23	0.4
tsw34	1,132.0	1,169.2	37.2	0.23	0.4
tsw35	1,030.6	1,132.0	101.4	0.32	0.4

NOTES:

1. Sensitivity analyses varied the AFM γ parameter between values of zero (all fractures accessible), 0.4, and 1.0 (maximum focusing).
2. The value of γ = 0.4 for the tsw31 unit is used in this response for consistency with the original FEHM simulations described in SAR Sections 2.3.5.3.2 and 2.3.5.3.3, and SNL 2007a, Sections 6.3.2.3 and 6.3.2.4.4. A value of γ = 0.088 is used for corresponding simulations with the UZ flow model (SNL 2007b, Table B-2).
3. Matrix diffusion coefficient = 3.74×10^{-11} m^2/s for all units, in all simulations.

Table 2. Hydrologic Properties for All FEHM and T2R3D Simulations Presented

Hydrologic Unit	Fracture Porosity	Fracture Permeability (m^2)	α_F (m^{-1}) (Note 1)	vG n_F (Note 2)	Fracture Residual Saturation	Matrix Porosity	Matrix Permeability (m^2)	α_M (m^{-1}) (Note 1)	vG n_M (Note 2)	Matrix Residual Saturation
tsw31	0.0050	8.1×10^{-13}	0.204	2.7248	0.01	0.043	3.21×10^{-17}	0.284	1.272 [3]	0.21
tsw32	0.0083	7.1×10^{-13}	0.554	2.7248	0.01	0.146	3.01×10^{-16}	0.156	1.408	0.07
tsw33	0.0058	7.8×10^{-13}	15.5	2.7248	0.01	0.136	1.86×10^{-17}	0.064	1.395	0.12
tsw34	0.0085	3.3×10^{-13}	3.10	2.7248	0.01	0.090	3.16×10^{-18}	0.0168	1.464	0.19
tsw35	0.0096	9.1×10^{-13}	5.64	2.7248	0.01	0.115	1.11×10^{-17}	0.0331	1.276	0.12

NOTES:

1. Capillary parameter (reciprocal air-entry pressure) in the van Genuchten (1980) equation for capillary pressure, for matrix (α_M) and fractures (α_F).
2. Dimensionless “n” in the van Genuchten (1980) equation for capillary pressure, for matrix (n_M) and fractures (n_F).
3. A value of 1.279 is used in the UZ flow model, and for the T2R3D simulations presented in this response.

Table 3. Summary of Fracture-Matrix Interaction Simulations Presented in Figure 1

Transport Code/Application	Tracer Release	Release Point(s)	Discussion
FEHM / transient breakthrough	Instantaneous Pulse	Fractures; top of column	Presented in SAR Figure 2.3.5-16; used to estimate effective residence time for fracture-matrix solute interaction in the NFC model
T2R3D / transient breakthrough	Instantaneous Pulse	Fractures; top of column	Alternative to FEHM simulations

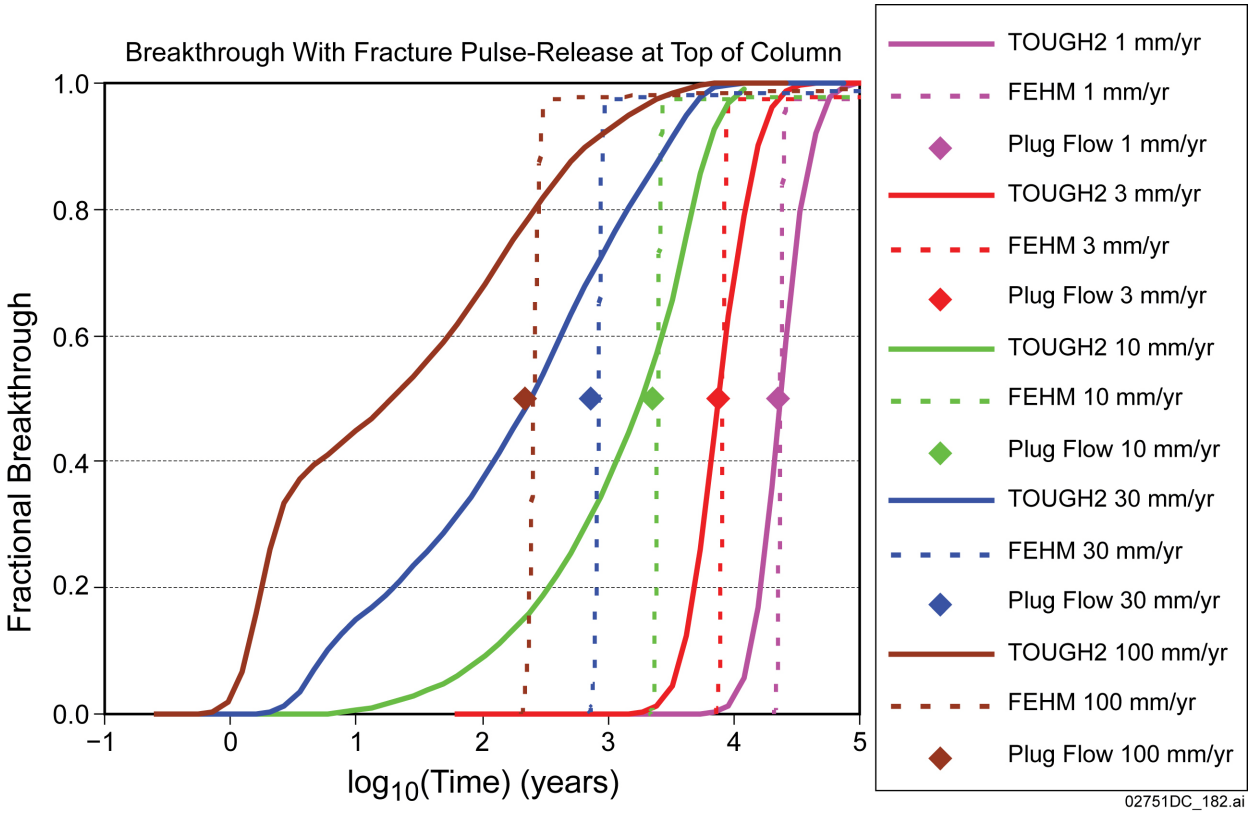

Figure 1. Original FEHM Breakthrough Simulations and Recalculated T2R3D Simulations (γ = 0.4) with Instantaneous Pulse Release in Fractures at the Top of the Column, and Fluxes of 1, 3, 10, 30, and 100 mm/yr, Plotted with Uncalibrated Plug-Flow Points from NFC Model

Table 4. Effective Residence Time Calibration with FEHM and T2R3D Transport Simulations

Percolation Flux (mm/yr)	Plug-Flow Residence Time Based on Percolation Flux (yr)	Calibrated Using Original FEHM Runs (TSPA-LA) (yr)	T2R3D Recalculated Median Residence Time (yr)	Difference of Recalculated vs. Original Calibrated Results (%)
1	22,224	23,484	23,578	0.4
3	7,408	8,170	7,626	−6.7
10	2,222	2,494	1,871	−25.0
30	741	840	241	−71.3
100	222	258	19	−92.6

All of the simulations discussed here, including the original work supporting the NFC model, were generated for ranges of percolation flux from 1 to 100 mm/yr, thereby addressing the impact of variable flow rates. Trend extrapolation is used in the NFC model for limited application to percolation flux values greater than 100 mm/yr (SNL 2007a, Section 6.3.2.4.4). All of the simulations were performed with zero longitudinal and transverse dispersivities, which is appropriate given that matrix diffusion has a much greater effect on tracer transport than does dispersion.

As shown in Figure 1 and Table 4, breakthrough times for the T2R3D simulations are similar to the FEHM results up to a percolation flux of approximately 10 mm/yr, and then decrease relative to the FEHM results for flux greater than 10 mm/yr. The breakthrough curves in Figure 1 are distributions of tracer residence time for the boundary condition of instantaneous fracture release (pulse, top of column). “Tailing” of the breakthrough curves increases for simulations at higher flux values. This dispersive “tailing” is caused mostly by the retarding effect of matrix diffusion. Residence time dispersion is not important to the use of calculated average or median residence times from these curves because fracture-matrix interaction is a spatially and temporally continuous process. The effect of matrix diffusion on the composition of seepage water is, therefore, represented by a convolution of breakthrough curves such as those presented here, with a continuous source function. The result is mixing of the effects from the upper and lower tails of the residence time distributions, in a manner that produces a net result that can be represented by an average or median residence time.

1.3 IMPACT EVALUATION FOR RECALCULATED RESIDENCE TIMES

The impact of adjusting the effective residence times in the NFC model using the T2R3D simulations is limited because the greatest relative difference (percent change in Table 4) is associated with higher flux conditions for which water-rock interaction is small relative to lower percolation flux conditions. To evaluate the impact on in-drift chemistry, median values for the T2R3D breakthrough curves were used to recalibrate the effective residence times in the NFC model (i.e., percolation flux values used in a “plug-flow” calculation), and the NFC model was rerun using the new percolation flux values to generate a new response surface (“map”) for the water–rock interaction parameter (WRIP). Median breakthrough times were used instead of mean breakthrough times as was done originally for the NFC model, because the means for the

T2R3D breakthrough curves at higher flux values are skewed to larger values by "tailing" behavior. The choice of median values is conservative for this comparison in the sense that it produces less fracture-matrix interaction for these conditions, thus enhancing the possibility of disequilibrium, and is more consistent with the quasi-steady state assumption inherent to the effective residence time approximation.

The WRIP values for the highest thermal measure, a matrix consisting of 102 rows representing time steps, by 20 columns representing a set of percolation flux histories, were then used to sample the NFC model EQ3/6 output files used to generate the pickup files for the seepage evaporation abstraction. These output files parametrically describe seepage water chemistry as a function of WRIP, drift wall temperature, and starting water. The same procedure was followed for both the original WRIP map used in the TSPA-LA, and the new map generated with T2R3D results. The results are shown in Figure 2, which compares the compositions of seepage water through time, for selected percolation flux histories in the WRIP map, for the hottest waste package location in the repository as represented for the NFC model. The percolation flux histories plotted in Figure 2 are provided in Table 5.

Examination of Figure 2 indicates there is little difference in predicted water chemistry (dotted lines on Figure 2) at low percolation flux values, for which breakthrough times are closely similar to values used for the TSPA-LA (solid lines on Figure 2). For percolation flux histories 1 and 2 the dotted lines and the solid lines plot are superposed on the figure. Differences in key chemical species (calcium, potassium, and pH are plotted) increase at higher flux values (above 10 mm/yr) during the thermal pulse, but are limited to a few parts per million in concentration (or a small fraction of a pH unit). At a later time during repository cooling, the differences decrease significantly. At the highest percolation flux values (30 mm/yr and higher), there is relatively little reaction between the rock and the downward moving water, although the effects of heating (e.g., calcite precipitation) are still observed.

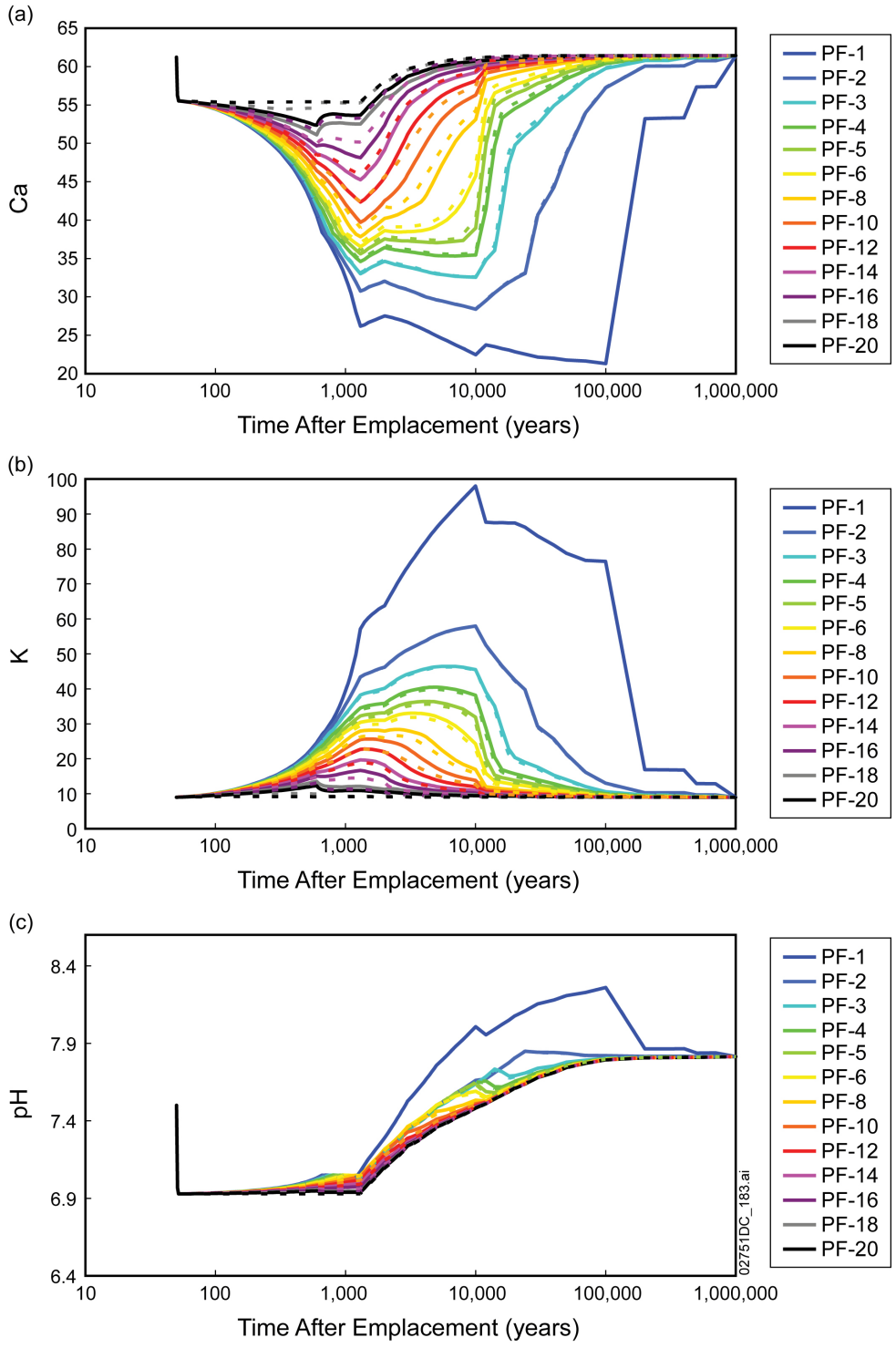

NOTE: Solid lines represent the original results used in the TSPA-LA, and dotted lines are results using T2R3D. “PF” refers to percolation flux histories 1 through 20, used in the NFC model. Percolation flux histories are given in Table 5.

Figure 2. Comparison of Seepage Water Compositions using the NFC Model with Adjusted Residence Time Based on Recalculated T2R3D Simulations for: (a) Calcium, (b) Potassium, and (c) pH

Table 5. Percolation flux sets Used in the Near Field Chemistry Model.

		Percolation Flux (mm/yr)			
ID # From NFC Model	**Percentile**	**Present-Day**	**Monsoon**	**Glacial Transition**	**Post-10 kyr**
1	0.025	0.05	0.28	0.05	0.19
2	0.075	0.37	1.14	0.50	1.22
3	0.125	0.86	2.11	1.06	2.66
4	0.175	1.41	3.35	1.67	4.34
5	0.225	2.10	4.50	2.39	5.93
6	0.275	2.79	5.62	3.37	7.79
8	0.375	4.49	7.78	5.85	13.25
10	0.475	6.47	10.15	9.35	19.15
12	0.575	9.22	13.47	14.76	25.33
14	0.675	12.61	19.21	22.99	35.63
16	0.775	17.38	29.03	36.06	52.09
18	0.875	28.09	73.59	58.00	66.88
20	0.975	44.19	119.94	102.33	93.46

1.4 SUMMARY

The effect of fast fracture-flow pathways on fracture-matrix interaction is represented using the AFM. Calculated tracer breakthrough time is equivalent to an effective residence time for fracture-matrix interaction. The extent of water–rock interaction is represented in the NFC model using an effective residence time approximation, calibrated to numerical simulations of tracer breakthrough. This approach is based on a quasi-steady state assumption, and is an appropriate simplification that has been used previously in the technical literature. Breakthrough curves were calculated using the T2R3D code to correct errors in the specification of fracture parameters and to use the AFM in flow calculations as well as tracer transport. These breakthrough curves were then used to recalibrate effective residence time in the NFC model. An evaluation of the impact on the chemistry of seepage waters from using the recalculated curves shows that concentrations of chemical constituents changed by a few ppm, and that the impact is limited in duration to the thermal pulse. These results show that the plug-flow feature of the NFC model, when calibrated to numerical results that include rapid breakthrough behavior at higher percolation flux values, is a reasonable approximation for the effective residence time or transport velocity of solute in waters percolating through the host rock.

2. COMMITMENTS TO NRC

The DOE commits to correct errors in SAR Section 2.3.5.3 as indicated in Section 3 below and consistent with the discussion and analysis presented in Section 1. These changes to the license application will be included in a future license application update.

3. DESCRIPTION OF PROPOSED LA CHANGE

- Correct SAR Section 2.3.5.3.2.2.1 (p. 2.3.5-30) to reflect the use of the T2R3D simulations and the additional analysis consistent with this RAI response.

- Correct the residence time adjustments in SAR Section 2.3.5.3.2.2.2 (p. 2.3.5-34) to those based on T2R3D simulations as presented in this RAI response.

- Correct the description of the residence time adjustments in SAR Section 2.3.5.3.3.2.7 (pp. 2.3.5-43 and -44) and include in this SAR section the interpretation of fast pathway effects on residence time as presented in this RAI response.

- Correct Figure 2.3.5-16 of the SAR by showing the results of the T2R3D-produced breakthrough times.

- Correct the summary of tracer transport simulations used to support the NFC model in SAR Section 2.3.5.3.3.5.5 (p. 2.3.5-65) to be consistent with the analysis presented in this RAI response.

4. REFERENCES

SNL (Sandia National Laboratories) 2007a. *Engineered Barrier System: Physical and Chemical Environment*. ANL-EBS-MD-000033 REV 06. Las Vegas, Nevada: Sandia National Laboratories. ACC: DOC.20070907.0003; LLR.20080328.0031.

SNL 2007b. *UZ Flow Models and Submodels*. MDL-NBS-HS-000006 REV 03 AD 01. Las Vegas, Nevada: Sandia National Laboratories. ACC: DOC.20080108.0003; DOC.20080114.0001; LLR.20080414.0007; LLR.20080414.0033; LLR.20080522.0086.

SNL 2008. *Particle Tracking Model and Abstraction of Transport Processes*. MDL-NBS-HS-000020 REV 02 AD 02. Las Vegas, Nevada: Sandia National Laboratories. ACC: DOC.20080129.0008; DOC.20070920.0003; LLR.20080325.0287; LLR.20080522.0170; LLR.20080603.0082.

van Genuchten, M.T. 1980. "A Closed-Form Equation for Predicting the Hydraulic Conductivity of Unsaturated Soils." *Soil Science Society of America Journal*, 44, (5), 892-898. Madison, Wisconsin: Soil Science Society of America.

RAI: Volume 3, Chapter 2.2.1.3.4, First Set, Number 3, Supplemental:

Justify the assumption that crack surface areas for HLW glass in the seismic scenario and under conditions of glass alteration are the same as those for the nominal case scenarios.

Also, provide bases for the assumption that only half of the cracked surfaces would be exposed to water vapor during dissolution in the vapor-phase aqueous environment.

Basis: The exposed surface area of the glass is important in assessing the radionuclide release from the glass dissolution. The applicant modeled surface area increase from cracking during vitrification in SAR 2.3.7.9.3 (and BSC 2004c, Section 6.6, Table 6-14). The exposure (i.e., increase) factor was represented by a triangular distribution with values from 4 to 17 (maximum probability at 4) in the nominal case (Table 2.4-11, SAR 2.4-400). The applicant estimated this distribution from the thermal cracking during the vitrification, the probability-weighted cracking from inadvertent handling, and the accessibility of water to tight cracks. However, the applicant did not provide the exposure factor under seismic conditions. Under seismic conditions there could be additional cracking. Under both nominal and seismic conditions, the applicant did not consider additional cracking due to potential volume increase of glass alteration products. The intact portion of glass may be subject to stress induced by the expansion of the alteration products during the glass dissolution (Abrajano, et al, 1990).

The bases for DOE's assumption that only half of the cracked surface would be exposed to vapor phase for inducing hydration and subsequent radionuclide release is unclear. Exposure to more than half the cracked surface area would seem to increase release rates; therefore, this assumption seems to be potentially non-conservative. It is also unclear whether more surface area releases both high solubility radionuclides (e.g., dissolved Tc-99) and low solubility radionuclides (e.g., Pu-239 colloids). The requested information is needed to verify compliance with 10 CFR 63.21(c)(9), (12) and (15) and 63.114(b) and (g).

1. RESPONSE

The probability-weighted effects of seismic cracking on the exposure factor uncertainty distribution are negligible. The approach involves considering the effects of seismic-induced impacts (between the codisposal packages and other packages, between the codisposal packages and their support pallets, and between the codisposal packages and the drip shield) (SNL 2007, Sections 6.4.6 and 6.4.7). The effects of these events on glass cracking are addressed by considering the bounding (most severe) event probabilities and comparing the range of seismic impact velocities for these bounding events to the velocities of drop impacts that were used in establishing the crack surface areas for the nominal case (Smith and Ross 1975, Figure 41). *Impact Testing of Vitreous Simulated High-Level Waste in Canisters* (Smith and Ross 1975,

Figure 41) provides experimental data showing the fractional increase in surface area as a function of impact velocity with an unyielding surface. These data show that the fractional increase in surface area is likely to be negligible for impacts associated with the more probable seismic events and small for the less probable and more severe seismic events.

The response builds on the justification provided in *Defense HLW Glass Degradation Model* (BSC 2004, Assumption 5.1), to "establish that the exposed surface area contacted by water is less than the calculated surface area, including the contribution of cracks." This response justifies the assumption that only half of the cracked surfaces are exposed in estimating the lower end of the uncertainty distribution range of the "exposure factor." It does so by discussing pertinent experimental data on the corrosion of glass with simulated and actual fracture surfaces.

The response also addresses the potential effects of volume expansion of glass corrosion products on glass cracking by discussing pertinent experimental data to show that this hypothetical process is not expected.

1.1 GLASS CRACKING EXPOSURE FACTOR UNCERTAINTY DISTRIBUTION FOR SEISMIC CASES

Seismic-induced impacts of Engineered Barrier System (EBS) components can occur due to asynchronous movement of the EBS components in response to vibratory ground movement (SNL 2007). Impact velocities (between waste packages, between codisposal packages and their support pallets, and between codisposal packages and the drip shield) are available based on analysis of the kinematic response of the EBS components to seismic events (SNL 2007, Section 6.3). Separate kinematic calculations were performed for 17 ground motion time histories for each of four seismic peak ground velocity (PGV) levels. The four PGV levels and their annual exceedance probabilities are: 10^{-4} per year for PGV level of 0.4019 m/s, 10^{-5} per year for PGV level of 1.05 m/s, 4.5×10^{-7}per year for PGV level of 2.44 m/s, and 10^{-8} per year for PGV level of 4.07 m/s (SNL 2007, Section 6.1, p. 6-2), as shown in Table 1. Because the range of the waste package to waste package impact velocities is similar to the range of the impact velocities with the other EBS components (SNL 2007, Section 6.3), and because the effects of all of the impacts on glass cracking are treated as if they were impacts with an unyielding surface, the following discussion is limited to impacts of the codisposal packages with other waste packages because of the large masses involved. The maximum impact velocities calculated for each of the 17 time histories associated with each of these four PGV levels are summarized in *Mechanical Assessment of Degraded Waste Packages and Drip Shields Subject to Vibratory Ground Motion* (SNL 2007, Table F-5). Only one of the 17 time histories produced an impact (impact velocity of 0.394 m/s or 1.293 fps) at the 0.4019 m/s PGV level. For the other three PGV levels, most of the 17 time histories caused impacts. The average and maximum impact velocities for 17 ground motion time histories at each PGV level, as shown in Table 1, are used to assess the effects of seismic impacts on glass cracking.

Table 1. Impact Velocities Between a Codisposal Waste Package and a TAD-Bearing Waste Package

Annual Exceedance Probability	PGV (m/s)	Average Impact Velocity (m/s)	Average Impact Velocity (ft/s)	Maximum Impact Velocity (m/s)	Maximum Impact Velocity (ft/s)
10^{-4}	0.40	0.394	1.293	0.394	1.293
10^{-5}	1.05	0.755	2.476	2.148	7.047
4.5×10^{-7}	2.44	1.884	6.180	4.165	13.665
10^{-8}	4.07	3.485	11.433	9.637	31.617

Source of data that are averaged in this table: SNL 2007, Table F-5.

NOTE: TAD = transportation, aging, and disposal (canister).

Available testing results (Smith and Ross 1975) correlate the extent of glass cracking (specifically, the fractional increase in geometric area) due to impact with an unyielding surface to the impact velocity (Smith and Ross 1975, Figure 41). These test data show that the best estimate increase in surface area associated with glass cracking due to an impact velocity corresponding to the maximum value of about 32 fps (the maximum impact velocity value calculated at the 4.07 m/s PGV level) is expected to cause a fractional increase in surface area of about 120% (estimated from Smith and Ross 1975, Figure 41). Because such a bounding case is realized in only one of the 17 ground motion time histories at the 4.07 m/s PGV level (which has an annual exceedance probability of 10−8), this surface area increase is unlikely. The average of the maximum impact velocities for the 4.07 m/s PGV level (i.e., 11.433 fps) is expected to produce a fractional increase of about 15% (estimated from Smith and Ross 1975, Figure 41). This same figure shows that the fractional increase in surface area is about 25% for the bounding estimate of the maximum impact velocities (13.665 fps) at the 2.44 m/s PGV level (which has an annual exceedance probability of $4.5 \times 10-7$). Even for the more severe low probability seismic events, the expected glass cracking impacts are small; the impacts associated with the more probable seismic events that produce PGV values less than the 2.44 m/s PGV level cause correspondingly smaller fractional increases in the glass surface area. A 25% increase in the extent of cracking is small compared to the extent of cracking associated with cooling and handling, and therefore does not contribute significantly to the uncertainty distribution for the fexposure parameter. The more probable seismic events will cause impact velocities that are expected to be sufficiently low to result in a negligible increase in the extent of glass cracking. Therefore, the probability-weighted effects of seismic cracking on the glass exposure factor uncertainty distribution are expected to be negligible.

1.2 BASIS FOR ASSUMPTION OF EXPOSURE OF HALF OF CRACKED SURFACES

As described in *Defense HLW Glass Degradation Model* (BSC 2004, Section 5.1), and as implemented in calculating the range of the uncertainty distribution for the "exposure factor" ($f_{exposure}$) (BSC 2004, Section 6.5.4) for glass fracture surfaces, the high end of the range is based on assuming free access of water to all of the cracked surfaces and the low end of the range assumes that "50% of the crack surfaces are contacted by water and have a reaction rate that is 50% of the rate at the free surface of the glass."

Available data show that glass corrosion and leaching at fracture surfaces inside cracks is lower than the corresponding rates at exposed external surfaces (BSC 2004, Section 6.5.4) and has led to the conclusion that "the assumption that crack surfaces leach as readily as external surfaces is unduly conservative" (BSC 2004, Section 6.5.4). Experimental studies using different simulated crack widths showed that the extent to which the leaching at crack surfaces is reduced compared to the exposed external surfaces depends on the crack width (Perez and Westsik 1981). No leaching was observed from tight cracks, and the leaching from cracks with small openings was found to be less than the leaching from exposed surfaces (Perez and Westsik 1981). Results from larger-scale leaching tests conducted on as-cut samples from a 24-inch diameter canister containing thermally cracked glass showed that the leaching rate was within a factor of three times the rates measured on small size samples with a polished (600-grit) finish when only the area of the cut surfaces was used to calculate the leaching rate of the large-scale samples (Bickford and Pellarin 1987). The less than a factor of three increase observed in the leaching of these large-scale thermally cracked samples was attributed mostly to roughness of the cut surfaces, despite the fact that the samples included fracture surface areas estimated to be from 25 to 35 times the surface area of the unfractured monolith. This indicates that the fracture surfaces contributed little to the observed leaching rate.

The experimental observations described above can be attributed to limitations that the fracture openings impose on the rate of transport of water to support the hydrolysis reactions that corrode the glass at the fracture surfaces (i.e., to the fracture surface "accessibility" factor), or to the limitations imposed on the dissolution rate of the glass due to rapid silica saturation of the small volumes of water available inside the fractures (i.e., to the surface "reactivity" factor). Both factors are uncertain. The possible range of both factors for cracked surfaces is 0 to 1. The experimental results cited above indicate that the lower end of the range is close to 0 for very tight cracks but is somewhat larger for wider cracks. Because of uncertainty in the fracture widths in the glass logs and because the future evolution of the fracture widths is also uncertain, it is reasonable to use the value of 1 for both the "accessibility" and "exposure" factors in setting the upper end of the $f_{exposure}$ factor range (BSC 2004, p. 6-45). The assumption that the value is 0.5 (i.e., the midpoint of the possible range) for the "accessibility" and "exposure" factors in evaluating the lower end of the $f_{exposure}$ factor range (BSC 2004, p. 6-45) is reasonable given that the available data indicate that 0.5 probably conservatively overestimates the actual value.

1.3 EFFECTS OF GLASS ALTERATION PRODUCTS ON CRACKING

Corrosion products produced during glass corrosion exhibit a complex composition and structure/microstructure that varies with time (e.g., Abrajano et al. 1990; Crovisier et al. 1986). The estimated bulk density of the alteration products observed under vapor hydration test conditions indicate that the density of the alteration layers can be considerably less than (approximately half) the density of the corroding glass (Jiricka et al. 2001). This indicates that volume expansion associated with formation of alteration products in cracks could potentially cause additional glass fracturing. However, studies of the dissolution of basaltic glass in seawater indicate that volume conservation can occur during the corrosion process (Crovisier et al. 1986, p. 2988). Laboratory tests of cracked glass do not report evidence of cracking due to volume expansion of the glass corrosion products (note that, because glass is brittle, any crack deformation caused by the volume expansion of corrosion products should be observed quickly

in the reaction progress). To the contrary, available evidence (e.g., Pederson et al. 1983, Figure 6) indicates that volume expansion associated with corrosion of glass at the location of a crack did not cause propagation of the fracture. Instead, Pederson et al. (1983, Figure 6) show that the corrosion of the glass at the location of the crack produced a rounded pit in the glass surface; volume expansion of the corrosion products formed at the crack location did not cause the crack to propagate into the glass or cause fracturing of the glass around the corrosion pit.

1.4 SUMMARY

Seismic events can cause codisposal packages to impact emplacement pallets, drip shields, or other adjacent packages in the drifts. The bounding effects of these impacts on glass cracking are assessed by considering the range of calculated impact velocities of codisposal packages with adjacent packages. The effects of impacts within this range of velocities on glass cracking is assessed using experimental data that correlates the fractional increase in glass log cracking with impact velocities onto an unyielding surface. This shows that the fractional surface area increases are small and negligible for the more likely seismic events; even the more severe and unlikely seismic impacts cause only modest fractional surface area increases compared to the distribution range (4 to 17) for the nominal case. Therefore, use of the nominal case distribution range for the seismic case is appropriate.

The possible range of the exposure factor's value used in calculating the lower end of the $f_{exposure}$ range is 0 to 1. Use of a value of 0.5 is reasonable given the experimental evidence showing that use of a value near the upper end of the range would be overly conservative.

Additional glass cracking caused by volume expansion of glass corrosion products is not considered because available data indicate that glass corrosion at the location of a crack causes development of a wide pit in the glass rather than crack extension or additional glass fracturing and because experimental evidence for such a process is lacking.

2. COMMITMENTS TO NRC

None.

3. DESCRIPTION OF PROPOSED LA CHANGE

None.

4. REFERENCES

Bickford, D.F. and Pellarin, D.H. 1987. "Large Scale Leach Testing of DWPF Canister Sections." *Scientific Basis for Nuclear Waste Management X, Symposium held December 1-4, 1986, Boston, Massachusetts*. Bates, J.K. and Seefeldt, W.B., eds. 84, 509-518. Pittsburgh, Pennsylvania: Materials Research Society.

BSC (Bechtel SAIC Company) 2004. *Defense HLW Glass Degradation Model.* ANL-EBS-MD-000016 REV 02. Las Vegas, Nevada: Bechtel SAIC Company. ACC: DOC.20041020.0015; DOC.20050922.0002; LLR.20080408.0271; DOC.20081021.0002.

Crovisier, J.L.; Honnorez, J.; and Eberhart, J.P. 1987. "Dissolution of Basaltic Glass in Seawater: Mechanism and Rate." *Geochimica et Cosmochimica Acta*, *51*, (11), 2977-2990. Elmsford, New York: Pergamon.

Jiricka, A.; Vienna, J.D.; Hrma, P.; and Strachan, D.M. 2001. "The Effect of Experimental Conditions and Evaluation Techniques on the Alteration of Low Activity Glasses by Vapor Hydration." *Journal of Non-Crystalline Solids*, *292*, (1-3), 25-43. New York, New York: North-Holland.

Pederson, L.R.; Buckwalter, C.Q.; and McVay, G.L. 1983. "The Effects of Surface Area to Solution Volume on Waste Glass Leaching." *Nuclear Technology*, *62*, 151-158. Washington, D.C.: American Nuclear Society.

Perez, J.M., Jr. and Westsik, J.H., Jr. 1981. "Effects of Cracks on Glass Leaching." *Nuclear and Chemical Waste Management*, *2*, 165-168. New York, New York: Pergamon Press.

SNL (Sandia National Laboratories) 2007. *Mechanical Assessment of Degraded Waste Packages and Drip Shields Subject to Vibratory Ground Motion.* MDL-WIS-AC-000001 REV 00. Las Vegas, Nevada: Sandia National Laboratories. ACC: DOC.20070917.0006; DOC.20080623.0002; DOC.20081021.0001.

Smith, T.H. and Ross, W.A. 1975. *Impact Testing of Vitreous Simulated High-Level Waste in Canisters*. BNWL-1903. Richland, Washington: Battelle Pacific Northwest Laboratories.